Chemical Science

ROYAL SOCIETY OF CHEMISTRY

EDGE ARTICLE

View Article Online
View Journal | View Issue

Check for updates

Cite this: *Chem. Sci.*, 2022, **13**, 8829

All publication charges for this article have been paid for by the Royal Society of Chemistry

Received 1st June 2022
Accepted 28th June 2022

DOI: 10.1039/d2sc03066g

rsc.li/chemical-science

SrO-layer insertion in Ruddlesden–Popper Sn-based perovskite enables efficient CO_2 electroreduction towards formate†

Jing Zhao,‡[ab] Peng Zhang,‡[ab] Lulu Li,[ab] Tenghui Yuan,[ab] Hui Gao,[ab] Gong Zhang,[ab] Tuo Wang,[ab] Zhi-Jian Zhao[ab] and Jinlong Gong*[abcd]

Tin (Sn)-based oxides have been proved to be promising catalysts for the electrochemical CO_2 reduction reaction (CO_2RR) to formate ($HCOO^-$). However, their performance is limited by their reductive transformation into metallic derivatives during the cathodic reaction. This paper describes the catalytic chemistry of a Sr_2SnO_4 electrocatalyst with a Ruddlesden–Popper (RP) perovskite structure for the CO_2RR. The Sr_2SnO_4 electrocatalyst exhibits a faradaic efficiency of 83.7% for $HCOO^-$ at −1.08 V *vs.* the reversible hydrogen electrode with stability for over 24 h. The insertion of the SrO-layer in the RP structure of Sr_2SnO_4 leads to a change in the filling status of the anti-bonding orbitals of the Sn active sites, which optimizes the binding energy of *OCHO and results in high selectivity for $HCOO^-$. At the same time, the interlayer interaction between interfacial octahedral layers and the SrO-layers makes the crystalline structure stable during the CO_2RR. This study would provide fundamental guidelines for the exploration of perovskite-based electrocatalysts to achieve consistently high selectivity in the CO_2RR.

Introduction

The electrochemical CO_2 reduction reaction (CO_2RR) is an attractive and sustainable approach to mitigate the greenhouse effect by storing renewable energy (*e.g.*, solar and wind energy) in the form of chemical bonds.[1–3] The CO_2RR can yield a variety of valuable products, among which formate ($HCOO^-$) shows the advantages of environmental compatibility and transportability as an important raw material.[4,5] It is also a promising material for liquid hydrogen storage for fuel cell applications.[5,6] $HCOO^-$ production by the CO_2RR has been proved to be predominately realized by tin(Sn)-based electrocatalysts.[7–12] The emerging evidence suggested that Sn oxides exhibit high activity.[7,13] Besides, Sn-based electrocatalysts have the advantages of low cost, abundance in the earth's crust and environmental friendliness.[7–9] Nevertheless, their selectivity to $HCOO^-$ would drop with the proceeding of the CO_2RR due to their reductive transformation into metallic derivatives.[14,15] Thence, there is an urgent need to design Sn-based oxides with consistently high selectivity.

The electrocatalytic performance of Sn-based oxides can be promoted through compositional and structural engineering, which can tune the electrical properties and coordination stability of the active sites.[16–19] For instance, N doping had been conducted to regulate the charge density of the Sn active sites in SnO_2 to enhance the selectivity towards $HCOO^-$.[19] Besides, $SrSnO_3$ has been proved to show high performance for the CO_2RR to $HCOO^-$ as a result of the perovskite structure.[16] However, the stability of $SrSnO_3$ is still not satisfactory. The deactivation mechanism of such ABO_3 perovskite electrocatalysts was proposed to be the surface amorphization or reconstruction during the electrocatalytic processes.[20–22] Therefore, effective strategies to stabilize the crystal structures of perovskites would help further enhance the performance of Sn-based electrocatalysts. The insertion of rock-salt AO-layers in Ruddlesden–Popper (RP) perovskite not only induces interlayer interaction to stabilize the crystal structure, but also optimizes the electrical properties of the active B-site.[23–26]

This paper describes the design and synthesis of two-dimensional layered Sr_2SnO_4 with a RP structure for the selective conversion of CO_2 to $HCOO^-$. Compared with the SnO_2 and $SrSnO_3$ samples, Sr_2SnO_4 shows enhanced selectivity with the Faradaic Efficiency (FE) for $HCOO^-$ reaching 83.7% (−1.08 V *vs.* the reversible hydrogen electrode). Besides, Sr_2SnO_4 exhibits long-term stability for over 24 h. As revealed by the experiments and density functional theory (DFT) calculations, the SrO-layer in the RP structure is the key to achieving good performance,

---

[a] *School of Chemical Engineering & Technology, Key Laboratory for Green Chemical Technology of Ministry of Education, Tianjin University, Tianjin 300072, China. E-mail: jlgong@tju.edu.cn*

[b] *Collaborative Innovation Center for Chemical Science & Engineering (Tianjin), Tianjin 300072, China*

[c] *Haihe Laboratory of Sustainable Chemical Transformations, Tianjin 300192, China*

[d] *Joint School of National University of Singapore and Tianjin University, International Campus of Tianjin University, Binhai New City, Fuzhou 350207, China*

† Electronic supplementary information (ESI) available. See https://doi.org/10.1039/d2sc03066g

‡ These authors contributed equally to this work.

which could optimize the binding energy of *OCHO and promote structural stability.

Results and discussion

Structures of catalysts

Fig. 1a shows the X-ray diffraction (XRD) patterns of SnO_2, $SrSnO_3$, and Sr_2SnO_4, the diffraction peaks of which are readily indexed to tetragonal SnO_2 (*P*42*mnm*, JCPDS No. 41-1445), cubic $SrSnO_3$ (*Pm*3*m*, JCPDS No. 74-1298) and tetragonal Sr_2SnO_4 (*I*4/*mmm*, JCPDS No. 97-002-7114), respectively. No peak corresponding to other phases was detected, demonstrating the high phase purity of SnO_2, perovskite $SrSnO_3$, and RP perovskite Sr_2SnO_4 catalysts. The scanning electron microscopy (SEM) images reveal the porous structures of the samples (Fig. S1†). In addition, the electron dispersive X-ray spectroscopy (EDS) mappings exhibit uniform distributions of Sr, Sn, and O elements (Fig. S2 and S3†). To further confirm the formation of the RP phase, the high-resolution transmission electron microscopy (HRTEM) image of Sr_2SnO_4 was collected (Fig. 1b). The observed lattice fringes with a spacing of 0.28 nm and 0.20 nm correspond to the (110) and (200) planes of Sr_2SnO_4. The inset shows the result of fast Fourier transform (FFT) analysis of the HRTEM image, which further confirms the tetragonal structure of Sr_2SnO_4. Moreover, the selected area electron diffraction (SAED) pattern of Sr_2SnO_4 clearly reflects the tetragonally arranged diffraction spots of the [001] zone axes (Fig. 1c), consistent with the result of the HRTEM characterization.

Raman spectroscopy was used to investigate the differences in structures between the three Sn-based oxides (Fig. 1d). The bands centered at 472, 631 and 771 cm^{-1} of SnO_2 correspond to the vibration modes of E_g, A_{1g}, and B_{2g}, respectively.[27] The band of $SrSnO_3$ at 399 cm^{-1} corresponds to SnO_3 torsional mode, and the peak at 576 cm^{-1} is associated with Sn–O stretching vibrations, indicating the formation of $[SnO_6]$ octahedra.[28,29] The band of Sr_2SnO_4 located at 445 cm^{-1} is related to the vibration of the bridge Sr–O–Sn oxygen bond axis in A_{1g} symmetry along the *c* axis. This band shows the interactions between the perovskite layers and the rock-salt SrO-layers in the RP structure.[30] The differences in the crystal structures of the three oxides are illustrated in Fig. 1e. For $SrSnO_3$, Sr^{2+} ions occupy the A-sites, whereas Sn^{4+} ions form the corner-linked $[SnO_6]$ octahedra at the B-sites. Sr_2SnO_4 is composed of rock-salt SrO-layers and $SrSnO_3$ perovskite layers along the crystallographic *c*-axis direction. This alternating layered RP structure would lead to unique structural and electrical properties, which could be beneficial for promoting electrocatalytic performance.[31,32]

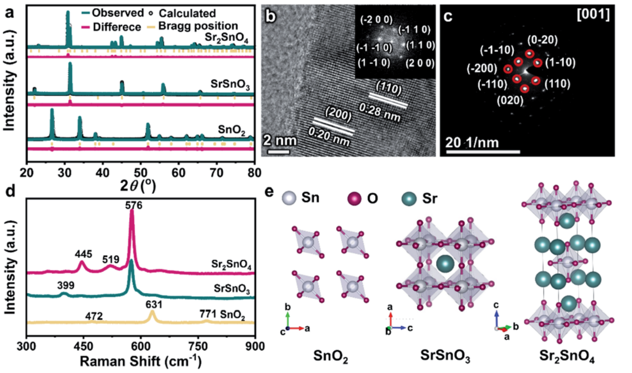

Fig. 1 (a) The XRD patterns of SnO_2, $SrSnO_3$, and Sr_2SnO_4 with their Rietveld refinement results. (b) HRTEM and FFT (inset) images of Sr_2SnO_4. (c) The SAED patterns along [001] of Sr_2SnO_4. (d) The Raman spectra of SnO_2, $SrSnO_3$, and Sr_2SnO_4. (e) Illustrations of the crystal structures of SnO_2, $SrSnO_3$, and Sr_2SnO_4. Color code: O (purple), Sr (turquoise), and Sn (gray).

CO_2RR performance

The CO_2RR performance was measured in a three-electrode H-type cell, with CO_2-saturated 0.5 M $KHCO_3$ as electrolyte. The products were analysed at potentials between −0.88 and −1.28 V *vs.* the reversible hydrogen electrode (RHE). All the following potentials are referred to the RHE. Sr_2SnO_4 exhibits a stable current density of up to 30.0 mA cm^{-2} at −1.28 V, surpassing those of the $SrSnO_3$ (22.9 mA cm^{-2}) and the SnO_2 (17.8 mA cm^{-2}) electrocatalysts (Fig. S4a, S5a, and S6†). The FE for $HCOO^-$ against potential over Sr_2SnO_4 shows a volcano trend, which first increases from 46.5% at −0.88 V to a peak value of 83.7% at −1.08 V. It then decreases to 62.7% at −1.28 V (Fig. 2a). The FEs for $HCOO^-$ over SnO_2 and $SrSnO_3$ also show similar volcano trends (Fig. S4b and S5b†), but with much lower peak values (64.6% for $SrSnO_3$ and 58.9% for SnO_2). Besides, Sr_2SnO_4 also exhibits the highest $HCOO^-$ partial current density of 12.4 mA cm^{-2} at −1.08 V compared to $SrSnO_3$ (9.0 mA cm^{-2}) and SnO_2 (5.9 mA cm^{-2}) (Fig. S7†). The stability tests were performed at a consistent potential of −1.08 V (Fig. 2c). Sr_2SnO_4 displays no obvious decay in the current density with the FE for $HCOO^-$ maintained at about 79.0%. However, there is an obvious increase in the current density for $SrSnO_3$ and SnO_2, with a decrease in $HCOO^-$ FE at the same time. Although the

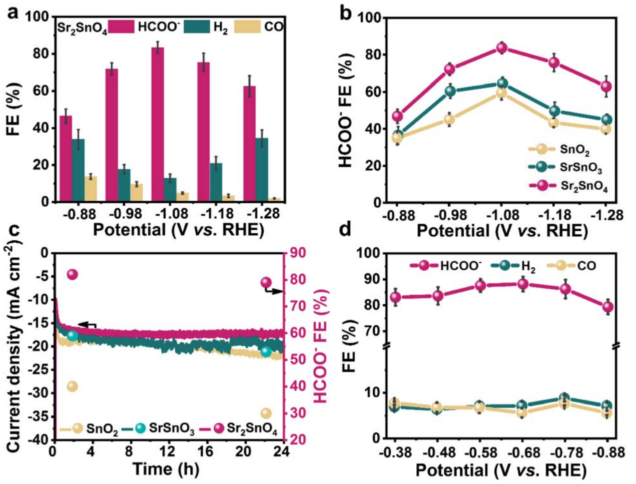

Fig. 2 (a) FEs for various products over Sr_2SnO_4. (b) FEs for $HCOO^-$ over SnO_2, $SrSnO_3$ and Sr_2SnO_4 at different potentials. (c) Stability tests of SnO_2, $SrSnO_3$ and Sr_2SnO_4 at a potential of −1.08 V *vs.* RHE. (d) FEs for various products over Sr_2SnO_4 in a flow cell.

selectivity of these Sn-based electrocatalysts may not reach the high value reported in some representative studies,[33,34] the comparison of their performance could reflect the structural advantages of the RP perovskite. The electrocatalytic performance of Sr_2SnO_4 was also evaluated in a flow cell with the catalysts dispersed on a gas diffusion electrode (GDE) to enhance the mass transfer of CO_2. The peak FE towards $HCOO^-$ over Sr_2SnO_4 is 84.5% at −0.68 V (Fig. 2d), and the current density for $HCOO^-$ reaches about 79.2 mA cm^{-2} at −0.88 V (Fig. S8†). Moreover, Sr_2SnO_4 displays long-term stability for over 50 h with the $HCOO^-$ partial current density maintained at about 59.1 mA cm^{-2} (Fig. S9†). The electrolyte was replaced during the chronoamperometric test to avoid the formation of (bi)carbonate salts on the diffusion layer, which caused the strong fluctuation of current density. The FEs towards H_2 and CO are below 10.0% with negligible change. According to the results of the activity evaluation, the Sr_2SnO_4 with the RP perovskite structure achieved consistently high selectivity towards $HCOO^-$. The performance of Sr_2SnO_4 is comparable to some of the state-of-the-art electrocatalysts for $HCOO^-$ production through the CO_2RR (Table S1†).

Operando Raman and ATR-SEIRAS spectra

To reveal the origin of the high stability of Sr_2SnO_4, *operando* Raman spectra of different samples were collected using a homemade electrochemical cell (Fig. S10†). With the decrease of the potential from −0.58 V to −1.28 V, the A_{1g} peak of crystalline SnO_2 at 631 cm^{-1} declines in intensity, which finally disappears after −1.08 V (Fig. 3a). This phenomenon would be caused by the reduction of SnO_2 to metallic Sn at high cathodic potentials, as proved by the formation of the Sn phase after the CO_2RR stability test (Fig. S11a†).[14] In the *operando* Raman spectra of $SrSnO_3$, the appearance of peaks at 631 cm^{-1} below −1.08 V suggests the surface reconstruction of $SrSnO_3$ to form SnO_2 during the CO_2RR, which would then be partially reduced to metallic Sn (Fig. 3b). This result could be supported by the XRD pattern of $SrSnO_3$ after the stability test, which clearly shows the presence of SnO_2 and Sn phases (Fig. S11b†).[16] In contrast, the Raman bands of Sr_2SnO_4 at 445 cm^{-1} arising from the interactions between the perovskite layer and rock-salt SrO-layer remain unchanged at different potentials, same as the bands corresponding to the $[SnO_6]$ octahedra at 576 cm^{-1} (Fig. 3c). These phenomena are in agreement with the end-of-test XRD pattern, showing diffraction peaks of only Sr_2SnO_4 (Fig. S11c†). The HRTEM and SEM images of the three Sn-based oxide catalysts after the CO_2RR stability test have been characterized. There was a significant change in the morphology of SnO_2 (Fig. S12a†). Such a change could be ascribed to the reduction of SnO_2 to metallic Sn (Fig. S13†). Similar phenomena could also be found for $SrSnO_3$, which could be reduced to SnO_2 and Sn (Fig. S12b and S14†). However, the morphology of the Sr_2SnO_4 electrocatalyst was maintained after the CO_2RR stability test (Fig. S12c†). Besides, the HRTEM image showed that the crystalline nature of Sr_2SnO_4 was maintained (Fig. S15†). EDS mappings of Sr_2SnO_4 after the stability test exhibit uniform distributions of Sr, Sn, and O elements (Fig. S16†). The results above demonstrate the superior stability of Sr_2SnO_4 during the CO_2RR. The high durability of Sr_2SnO_4 would be induced by the SrO-layer insertion in the RP structure, which leads to the strong interaction between perovskite layers and rock-salt SrO-layers to prohibit structural deformation and reconstruction.[26]

In addition to good stability, the RP perovskite Sr_2SnO_4 electrocatalyst shows high selectivity towards $HCOO^-$. To find the underlining mechanism of the promoted electrocatalytic performance, *operando* attenuated-total-reflection surface-enhanced infrared absorption spectroscopy (ATR-SEIRAS) characterization was conducted. The peaks at around 1630 cm^{-1} observed in all three samples can be assigned to the interfacial H_2O (Fig. 4a–c).[9,35] The bands at 1367–1358 cm^{-1}, 1397–1390 cm^{-1} and 1390–1386 cm^{-1} for SnO_2, $SrSnO_3$ and Sr_2SnO_4 with an obvious Stark effect (peak position shifted to a lower wavenumber at more negative potentials) could be assigned to *OCHO absorbed on the surface.[36,37] The *OCHO peaks of SnO_2 can be observed from −0.48 V to −1.28 V. For $SrSnO_3$, the signal of *OCHO appears at −0.68 V and disappears at −1.18 V. The signal of *OCHO was detected from −0.58 V to −0.88 V for Sr_2SnO_4. Since *OCHO is the essential intermediate for the generation of $HCOO^-$,[38] its rapid desorption on Sr_2SnO_4 would be the result of the weak adsorption of *OCHO, considering its high selectivity towards $HCOO^-$.[39,40] Therefore, the high selectivity of Sr_2SnO_4 would originate from the optimized binding energy of *OCHO on the surface, which might be realized by the SrO-layer insertion in the RP perovskite structure.

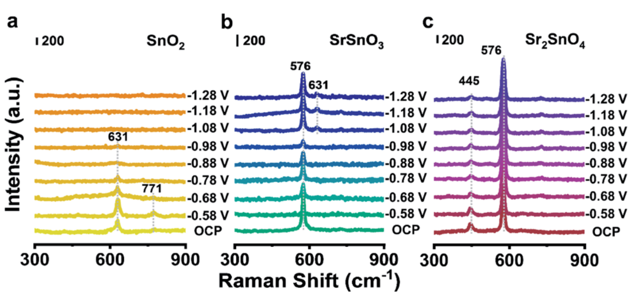

Fig. 3 *Operando* Raman spectra of (a) SnO_2, (b) $SrSnO_3$ and (c) Sr_2SnO_4 recorded at various potentials *vs.* RHE in a CO_2-saturated 0.5 M $KHCO_3$ solution, respectively.

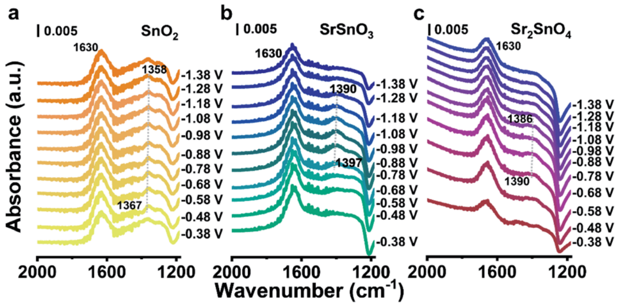

Fig. 4 *Operando* ATR-SEIRAS spectra of (a) SnO_2 (b) $SrSnO_3$ and (c) Sr_2SnO_4 recorded at various potentials *vs.* RHE in a CO_2-saturated 0.5 M $KHCO_3$ solution, respectively.

DFT simulations

To further reveal the intrinsic role of the RP structure of Sr_2SnO_4 in promoting selectivity, DFT simulations were performed. Thermodynamically stable SnO_2(110),[41] $SrSnO_3$(001) (Table S2†) and SrO-terminated Sr_2SnO_4(002) surfaces[24] were chosen as the starting models for the computational study. The influence of surface vacancies, which significantly affect the surface catalytic reactions, was considered due to the relatively large energy required for the formation of bulk oxygen vacancies in these samples (Tables S3 and S4†). According to their surface phase diagrams (Fig. S17†), $SnO_2(110)/4O_{bri}H^*$,[41] $SrSnO_3$(001)/7Ov and Sr_2SnO_4(002)/8Ov were found to be stable in the CO_2RR process. These models were selected for the understanding of the reaction mechanism, which would represent the real active sites of the catalysts during the reaction. As shown in the well-discussed reaction pathway of the CO_2RR to $HCOO^-$ (Fig. S18†), the *OCHO intermediate is formed by the hydrogenation of CO_2, which subsequently produces HCOOH by the transfer of electrons and protons.[41,42] The results of DFT simulations show that the formation energy of *OCHO over the Sr_2SnO_4(002)/8Ov surface (0.20 eV) is higher than those over the $SrSnO_3$(001)/7Ov and the SnO_2(110) (Fig. 5a). The process of *OCHO desorption to form HCOOH on Sr_2SnO_4(002)/8Ov is spontaneous. However, the energy barriers for *OCHO desorption over SnO_2(110) and $SrSnO_3$(001)/7Ov are around 0.70 eV and 0.39 eV. Therefore, Sr_2SnO_4 undergoes easy desorption of *OCHO for the CO_2RR to $HCOO^-$, which is in accordance with the results of the *operando* ATR-SEIRAS characterization. Besides, the ΔG_{H^*} on Sr_2SnO_4(002)/8Ov is higher than those on the $SrSnO_3$(001)/7Ov and the SnO_2(110) (Fig. 5b), as reflected by the relatively low selectivity towards H_2 on Sr_2SnO_4 (Fig. 2a, S4b and S5b†). Since the thermodynamically stable SrO-layer in Sr_2SnO_4(002) may be involved in the reaction (Fig. S19†), its role in the CO_2RR was investigated, which would also promote *OCHO generation and inhibit H_2 production (Fig. S20†). These results indicate that Sr_2SnO_4 exhibits high selectivity due to the optimized binding strength of *OCHO.

Furthermore, crystal orbital Hamilton population (COHP) analysis was conducted to explore how the SrO-layer insertion in Sr_2SnO_4 would affect the selectivity (Fig. 5c). The anti-bonding orbitals of Sn active sites with the O atom of *OCHO below the Fermi level (E_f) imply the weakening adsorption of *OCHO on Sn, which is most obvious on the Sr_2SnO_4(002) surface. Therefore, the filling of the anti-bonding orbitals leads to a reduction in the bonding strength of Sn–O, corresponding to the relatively weak adsorption strength of *OCHO on Sr_2SnO_4. Besides, the linear relationship between the integrated COHP (iCOHP) and ΔG_{*OCHO} quantitatively confirms that the population of bonding/antibonding orbitals below E_f is the key factor in regulating the ΔG_{*OCHO} (Fig. 5d).[41] Therefore, the tuned electrical properties of active sites in the RP perovskite Sr_2SnO_4 electrocatalyst optimize the binding energy of *OCHO over Sr_2SnO_4(002)/8Ov, leading to the high selectivity for the CO_2RR to $HCOO^-$.

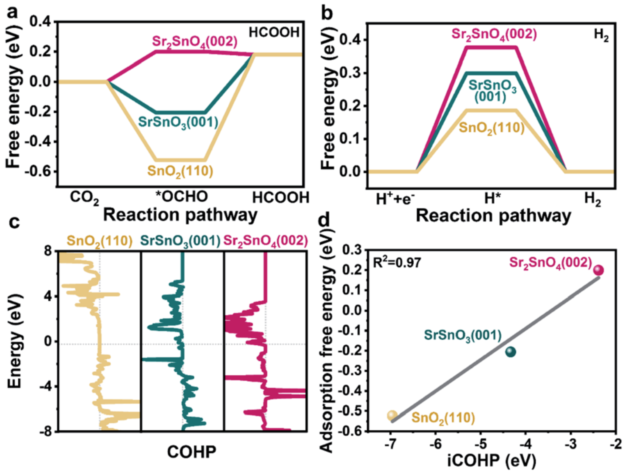

Fig. 5 The calculated free energy for (a) HCOOH and (b) H_2. (c) COHP curves of Sn active sites on SnO_2(110), $SrSnO_3$(001), and Sr_2SnO_4(002) with O of *OCHO interaction. (d) The correlation between the iCOHP and adsorption free energy of *OCHO on SnO_2(110), $SrSnO_3$(001), and Sr_2SnO_4(002).

Conclusions

In summary, a Sr_2SnO_4 perovskite electrocatalyst with a RP structure was fabricated *via* a simple solid-state reaction. Sr_2SnO_4 exhibits high performance for the CO_2RR with an FE of 83.7% towards $HCOO^-$ and long-term durability of over 24 h. The SrO-layer insertion in the RP structure leads to strong interlayer interactions, which could prohibit structural deformation and reconstruction. Thus, Sr_2SnO_4 possesses good stability. Besides, the anti-bonding orbital filling of the Sn active site in the RP structure results in the favorable binding strength of *OCHO on Sr_2SnO_4, so that it shows higher selectivity towards $HCOO^-$ than the SnO_2 and the $SrSnO_3$ control samples. Our work demonstrates that Sr_2SnO_4 can serve as an efficient electrocatalyst for $HCOO^-$ production through the CO_2RR. The findings would guide the rational design of perovskite-based electrocatalysts and open up an avenue for tuning the catalytic selectivity and stability by structure engineering.

Data availability

The data that supports the findings of this study is available from the corresponding author upon reasonable request.

Author contributions

J. L. G supervised the project. P. Z. and J. Z. conceived the idea. J. Z. synthesized the catalysts and conducted the CO_2RR performance tests. L. L. L conducted DFT simulations. Y. T. H., G. H., and G. Z. conducted related characterization studies. All the authors participated in the writing of the manuscript.

Conflicts of interest

There are no conflicts to declare.

Acknowledgements

We acknowledge the National Key R&D Program of China (2021YFA1501503), the National Natural Science Foundation of China (22121004, 22108197), the Haihe Laboratory of Sustainable Chemical Transformations (CYZC202107), the Natural Science Foundation of Tianjin City (18JCJQJC47500), the Program of Introducing Talents of Discipline to Universities (No. BP0618007) and the Xplorer Prize for financial support.

References

1 S. Zhang, Q. Fan, R. Xia and T. J. Meyer, *Acc. Chem. Res.*, 2020, **53**, 255–264.
2 X. Wang, Z. Wang, F. P. García de Arquer, C.-T. Dinh, A. Ozden, Y. Li, D.-H. Nam, J. Li, Y.-S. Liu, J. Wicks, Z. Chen, M. Chi, B. Chen, Y. Wang, J. Tam, J. Y. Howe, A. Proppe, P. Todorović, F. Li, T.-T. Zhuang, C. M. Gabardo, A. R. Kirmani, C. McCallum, S.-F. Hung, Y. Lum, M. Luo, Y. Min, A. Xu, C. P. O'Brien, B. Stephen, B. Sun, A. H. Ip, L. J. Richter, S. O. Kelley, D. Sinton and E. H. Sargent, *Nat. Energy*, 2020, **5**, 478–486.
3 Y. Ling, Q. Ma, Y. Yu and B. Zhang, *Trans. Tianjin Univ.*, 2021, **27**, 180–200.
4 X. An, S. Li, X. Hao, Z. Xie, X. Du, Z. Wang, X. Hao, A. Abudula and G. Guan, *Renew. Sustain. Energy Rev.*, 2021, **143**, 110952.
5 N. Han, P. Ding, L. He, Y. Li and Y. Li, *Adv. Energy Mater.*, 2020, **10**, 1902338.
6 S. Agarwal, Y. Zhai, D. Hill and N. Sridhar, *ChemSusChem*, 2011, **4**, 1301–1310.
7 Y. Chen and M. W. Kanan, *J. Am. Chem. Soc.*, 2012, **134**, 1986–1989.
8 R. Daiyan, E. C. Lovell, N. M. Bedford, W. H. Saputera, K.-H. Wu, S. Lim, J. Horlyck, Y. H. Ng, X. Lu and R. Amal, *Adv. Sci.*, 2019, **6**, 1900678.
9 W. Deng, L. Zhang, L. Li, S. Chen, C. Hu, Z.-J. Zhao, T. Wang and J. Gong, *J. Am. Chem. Soc.*, 2019, **141**, 2911–2915.
10 H. Li, N. Xiao, Y. Wang, C. Liu, S. Zhang, H. Zhang, J. Bai, J. Xiao, C. Li, Z. Guo, S. Zhao and J. Qiu, *J. Mater. Chem. A*, 2020, **8**, 1779–1786.
11 S. Lee, H. Ju, R. Machunda, S. Uhm, J. K. Lee, H. J. Lee and J. Lee, *J. Mater. Chem. A*, 2015, **3**, 3029–3034.
12 N. Han, Y. Wang, J. Deng, J. Zhou, Y. Wu, H. Yang, P. Ding and Y. Li, *J. Mater. Chem. A*, 2019, **7**, 1267–1272.
13 C. Liang, B. Kim, S. Yang, Y. Liu, C. F. Woellner, Z. Li, R. Vajtai, W. Yang, J. Wu, P. J. A. Kenis and P. M. Ajayan, *J. Mater. Chem. A*, 2018, **6**, 10313–10319.
14 A. Dutta, A. Kuzume, M. Rahaman, S. Vesztergom and P. Broekmann, *ACS Catal.*, 2015, **5**, 7498–7502.
15 R. Daiyan, X. Lu, Y. H. Ng and R. Amal, *Catal. Sci. Technol.*, 2017, **7**, 2542–2550.
16 Y. Pi, J. Guo, Q. Shao and X. Huang, *Nano Energy*, 2019, **62**, 861–868.
17 X. An, S. Li, A. Yoshida, T. Yu, Z. Wang, X. Hao, A. Abudula and G. Guan, *ACS Appl. Mater. Interfaces*, 2019, **11**, 42114–42122.
18 G. Wen, B. Ren, M. G. Park, J. Yang, H. Dou, Z. Zhang, Y.-P. Deng, Z. Bai, L. Yang, J. Gostick, G. A. Botton, Y. Hu and Z. Chen, *Angew. Chem., Int. Ed.*, 2020, **59**, 12860–12867.
19 C. Hu, L. Zhang, L. Li, W. Zhu, W. Deng, H. Dong, Z.-J. Zhao and J. Gong, *Sci. China Chem.*, 2019, **62**, 1030–1036.
20 N. Tsvetkov, Q. Lu, L. Sun, E. J. Crumlin and B. Yildiz, *Nat. Mater.*, 2016, **15**, 1010–1016.
21 Y. Chen, H. Li, J. Wang, Y. Du, S. Xi, Y. Sun, M. Sherburne, J. W. Ager III, A. C. Fisher and Z. J. Xu, *Nat. Commun.*, 2019, **10**, 572.
22 X. Xu, Y. Chen, W. Zhou, Z. Zhu, C. Su, M. Liu and Z. Shao, *Adv. Mater.*, 2016, **28**, 6442–6448.
23 J. Wang, C. Cheng, B. Huang, J. Cao, L. Li, Q. Shao, L. Zhang and X. Huang, *Nano Lett.*, 2021, **21**, 980–987.
24 Y. Zhu, H. A. Tahini, Z. Hu, J. Dai, Y. Chen, H. Sun, W. Zhou, M. Liu, S. C. Smith, H. Wang and Z. Shao, *Nat. Commun.*, 2019, **10**, 149.
25 C. Zhu, H. Tian, B. Huang, G. Cai, C. Yuan, Y. Zhang, Y. Li, G. Li, H. Xu and M.-R. Li, *Chem. Eng. J.*, 2021, **423**, 130185.
26 L.-F. Huang, N. Z. Koocher, M. Gu and J. M. Rondinelli, *Chem. Mater.*, 2018, **30**, 7100–7110.
27 S. Sun, G. Meng, G. Zhang, T. Gao, B. Geng, L. Zhang and J. Zuo, *Chem. Phys. Lett.*, 2003, **376**, 103–107.
28 M. Muralidharan, V. Anbarasu, A. Elaya Perumal and K. Sivakumar, *J. Mater. Sci.: Mater. Electron.*, 2017, **28**, 4125–4137.
29 U. Kumar and S. Upadhyay, *J. Electron. Mater.*, 2019, **48**, 5279–5293.
30 A. Magrez, M. Cochet, O. Joubert, G. Louarn, M. Ganne and O. Chauvet, *Chem. Mater.*, 2001, **13**, 3893–3898.
31 R. P. Forslund, W. G. Hardin, X. Rong, A. M. Abakumov, D. Filimonov, C. T. Alexander, J. T. Mefford, H. Iyer, A. M. Kolpak, K. P. Johnston and K. J. Stevenson, *Nat. Commun.*, 2018, **9**, 3150.
32 G. Nirala, D. Yadav and S. Upadhyay, *J. Adv. Ceram.*, 2020, **9**, 129–148.
33 Y. Hori, H. Wakebe, T. Tsukamoto and O. Koga, *Electrochim. Acta*, 1994, **39**, 1833–1839.
34 K. Bejtka, J. Zeng, A. Sacco, M. Castellino, S. Hernández, M. A. Farkhondehfal, U. Savino, S. Ansaloni, C. F. Pirri and A. Chiodoni, *ACS Appl. Energy Mater.*, 2019, **2**, 3081–3091.
35 W. Thornton and P. G. Harrison, *J. Chem. Soc., Faraday Trans.*, 1975, **71**, 461–472.
36 Y. Katayama, F. Nattino, L. Giordano, J. Hwang, R. R. Rao, O. Andreussi, N. Marzari and Y. Shao-Horn, *J. Phys. Chem. C*, 2018, **123**, 5951–5963.
37 Y. Liang, W. Zhou, Y. Shi, C. Liu and B. Zhang, *Sci. Bull.*, 2020, **65**, 1547–1554.
38 J. E. Pander, M. F. Baruch and A. B. Bocarsly, *ACS Catal.*, 2016, **6**, 7824–7833.
39 S. Zhu, B. Jiang, W.-B. Cai and M. Shao, *J. Am. Chem. Soc.*, 2017, **139**, 15664–15667.
40 J. Heyes, M. Dunwell and B. Xu, *J. Phys. Chem. C*, 2016, **120**, 17334–17341.
41 L. Li, Z.-J. Zhao, C. Hu, P. Yang, X. Yuan, Y. Wang, L. Zhang, L. Moskaleva and J. Gong, *ACS Energy Lett.*, 2020, **5**, 552–558.
42 J. S. Yoo, R. Christensen, T. Vegge, J. K. Nørskov and F. Studt, *ChemSusChem*, 2016, **9**, 358–363.